THE ASTROPHYSICAL JOURNAL, 503:744–759, 1998 August 20
© 1998. The American Astronomical Society. All rights reserved. Printed in U.S.A.

THE SPECTRUM OF TeV GAMMA RAYS FROM THE CRAB NEBULA

A. M. HILLAS,[1] C. W. AKERLOF,[2] S. D. BILLER,[1,3] J. H. BUCKLEY,[4,15] D. A. CARTER-LEWIS,[5] M. CATANESE,[5] M. F. CAWLEY,[6] D. J. FEGAN,[7] J. P. FINLEY,[8] J. A. GAIDOS,[8] F. KRENNRICH,[5] R. C. LAMB,[9] M. J. LANG,[12] G. MOHANTY,[5,13] M. PUNCH,[7,10] P. T. REYNOLDS,[4,10] A. J. RODGERS,[1] H. J. ROSE,[1] A. C. ROVERO,[14] M. S. SCHUBNELL,[2] G. H. SEMBROSKI,[8] G. VACANTI,[4,11] T. C. WEEKES,[4] M. WEST,[1] AND J. ZWEERINK[5]

Received 1997 July 10; accepted 1998 March 26

ABSTRACT

The spectrum of gamma rays from the Crab Nebula has been measured in the energy range 500 GeV–8 TeV at the Whipple Observatory by the atmospheric Cerenkov technique. Two methods of analysis that were used to derive spectra, in order to reduce the chance of calibration errors, gave good agreement, as did analysis of observations made with changed equipment several years apart. It is concluded that stable and reliable energy spectra can now be made in the TeV range. The spectrum can be represented in this energy range by the power-law fit, $J = (3.20 \pm 0.17 \pm 0.6) \times 10^{-7} \times (E/1\ \mathrm{TeV})^{-2.49 \pm 0.06 \pm 0.04}\ \mathrm{m^{-2}\ s^{-1}\ TeV^{-1}}$, or by the following form, which extends much better to the GeV domain: $J = (3.25 \pm 0.14 \pm 0.6) \times 10^{-7} E^{-2.44 \pm 0.06 \pm 0.04 - 0.151 \log_{10} E}\ \mathrm{m^{-2}\ s^{-1}\ TeV^{-1}}$ (E in TeV). The integral flux above 1 TeV is $(2.1 \pm 0.2 \pm 0.3) \times 10^{-7}\ \mathrm{m^{-2}\ s^{-1}}$. Using the complete spectrum of the Crab Nebula, the spectrum of relativistic electrons is deduced, and the spectrum of the inverse Compton emission that they would generate is in good agreement with the observed gamma-ray flux from 1 GeV to many TeV, if the magnetic field in the region where these scattered photons originate (essentially the X-ray–emitting region, around 0.4 pc from the pulsar) is $\sim$16 nT (160 μG), in reasonable agreement with the field deduced by Aharonian & Atoyan. If the same field strength were present throughout the nebula, there would be no clear need for an additional radiation source in the GeV domain such as has recently been suggested; the results give an indication that the magnetic field is well below the often-assumed equipartition strength (35–60 nT). Further accurate gamma-ray spectral measurements over the range from 1 GeV to tens of TeV have the potential to probe the growth in the magnetic field in the inner region of the nebula.

Subject headings: gamma rays: observations — ISM: individual (Crab Nebula) — ISM: magnetic fields — radiation mechanisms: nonthermal — supernova remnants

1. INTRODUCTION

Of the known cosmic sources of TeV gamma rays, the Crab Nebula is the only one in the northern sky to have an apparently steady output, and hence it has been observed the most extensively, with the objectives of refining the methods of observation in this new field and determining the energy spectrum of the radiation. This object has an extraordinarily broad spectrum, mostly attributed to synchrotron radiation from electrons apparently injected outside the cavity dominated by the pulsar wind with energies from GeV to a few PeV, but this continuous spectrum appears to terminate near 10^8 eV, and the GeV to TeV photons form a new component of the spectrum. Over most of the broad spectral range, additional pulsed radiation emerges from the central pulsar. This report is concerned with the steady flux of gamma rays, presumably not originating so close to the pulsar: we detect no pulsed component near 10^{12} eV (Gillanders et al. 1997). We have previously described how, using the 10 m telescope of the Whipple Observatory, it is possible to identify flashes of Cerenkov radiation in the upper atmosphere due to electron-photon cascades initiated by the incoming photons. In 1989 (Weekes et al. 1989) we were first able to obtain a signal from the Crab Nebula with a workable signal-to-noise ratio (S/N) of 9; then, using an improved camera (Vacanti et al. 1991), the S/N improved to 20 from 32 hr of observation on source and a similar off-source control, and refinements in technique improved the background rejection still further (Reynolds et al. 1993). Observations of this bright and steady source were crucial in improving the sensitivity and stability of the technique, with the result that flickering BL Lac objects can now be recorded with confidence. However, despite a continual improvement in sensitivity of the detec-

[1] Department of Physics and Astronomy, University of Leeds, Leeds LS2 9JT, UK.
[2] Randall Laboratory of Physics, University of Michigan, Ann Arbor, MI 48109-1120.
[3] Now at Department of Physics, University of Oxford, Oxford OX1 3RH, UK.
[4] Whipple Observatory, Harvard-Smithsonian Center for Astrophysics, PO Box 97, Amado, AZ 85645-0097.
[5] Department of Physics and Astronomy, Iowa State University, Ames, IA 50011-3160.
[6] Physics Department, St.Patrick's College, Maynooth, Ireland.
[7] Department of Experimental Physics, University College, Belfield, Dublin 4, Ireland.
[8] Department of Physics, Purdue University, West Lafayette, IN 47907.
[9] Space Sciences Laboratory, California Institute of Technology, Pasadena, CA 91125.
[10] Now at Laboratoire de Physique Corpusculaire, College de France, 75231 Paris, and IN2P3/CNRS, France.
[11] Astrophysics Division, ESA/ESTEC, Postbus 299, NL-2200, AG Nordwijk, Netherlands.
[12] Physics Department, University College, Galway, Ireland.
[13] Now at LPHNE, Ecole Polytechnique, Route de Saclay, 91128 Palaiseau Cedex, France.
[14] Instituto de Astronomia y Fisica del Espacio (CONICET) C.C. 67, Suc. 28, 1428 Buenos Aires, Argentina.
[15] Now at Department of Physics, Washington University in St Louis, St Louis, MO 63160.

tion technique, the derivation of an accurate flux of gamma rays from the Crab Nebula proved more difficult. Since the work of Vacanti et al. (1991), which used a rather simple analysis, some more detailed alternative analyses of the process of selection of "gammalike" events and of the deduced spectra produced considerably divergent results. This led us to explore several somewhat different methods of data analysis and simulation in order to understand the possible biases and errors. For this purpose the Crab Nebula has been studied thoroughly as the test case for developing methods of energy and flux calibration. In the end we have derived a flux from the Crab Nebula close to our previous simple estimate of 1991, though now with much better justification. We now feel confident in deriving spectra for other objects, such as Markarian 421. A detailed paper on our methods (Mohanty et al. 1998) explains two approaches to the derivation of the spectrum, based on independent shower simulation programs and alternative basic calibration standards (relying either on the best information about optical sensitivities and transmissions or on calibration of the whole detector against showers produced by the known flux of hadronic cosmic rays) and following different routes to the spectrum. In § 2 we give only a brief summary of these methods, and we present the results for the Crab Nebula. The implications of the results, which mainly concern the magnetic field strength in the nebula, are discussed in § 3.

2. PROCEDURES FOR DERIVING THE SPECTRUM

The basis for the detection of these gamma rays is that a photon entering the atmosphere soon gives its energy to an electron-positron pair, and there ensues an electron-photon cascade of narrow lateral extent, continuing forward in the same direction. About half of the electrons are traveling faster than light in air and emit Cerenkov radiation within a narrow cone of around 1° half-angle. The result is a pool of light on the ground, about 125 m in radius at the altitude of the Whipple Observatory, within which the light intensity is nearly uniform and nearly proportional to the energy in the shower (provided that one avoids the central 30 m, where there is a variable enhancement around the few particles that penetrate to the ground). At distances $r > 125$ m, the intensity falls off roughly as r^{-2}. Hence the energy of the gamma ray is determined by the intensity of the light flash, provided that one can ensure that it is detected within the right range of distance from the impact point on the ground of the initial trajectory, or, almost equivalently, within about 0.°4–1° of the source direction. The tasks of the analysis are to relate the detector response to light intensity (over a broad spectral range) and hence to the photon's energy, allowing for imperfect atmospheric transmission and for gradual changes in optical reflectivities, and to determine the efficiency with which the flashes are recorded for impact points at various distances from the telescope. This consideration of efficiency is not simple because it has proved highly profitable to impose tight selection criteria (known as "Supercuts") on the characteristics of flash images that are accepted, in order to reject other flashes from an overwhelming flux of cosmic-ray protons and nuclei, and it is thus necessary to be sure that the selection is retaining the gamma-ray flashes with a known efficiency and to know how this efficiency varies with energy. Even when gammalike images are selected, it is necessary to record flashes from the vicinity of the Crab Nebula and also from an "off-source" region of the sky, displaced 30^m in right ascension and observed at the same hour angle and altitude, in order to correct for the appreciable background of remaining flashes due to isotropic cosmic rays. The excess of counts "on source" over those seen "off source" is then attributed to uncharged radiation from the source (the Crab Nebula). Limited angular resolution does not permit us to distinguish between the pulsar and the nebula as a source.

Because some previous attempts to derive the spectrum of the Crab Nebula had produced notably different fluxes, two subgroups of the Whipple collaboration followed independent analyses that differed in detail at several points. Another paper (Mohanty et al. 1998) gives a fuller explanation of the different methods of analysis used to derive the energy spectrum, which may be paraphrased as follows.

Method 1.—A careful extension of previously well-explored methods: selection of gammalike images after modifying "Supercuts" to apply to a wide range of energies; laboratory optical calibrations; estimating the energy of each event; grouping the events by estimated energy; estimating the effective collecting area at each energy.

Method 2.—A variant of method 1, the differences being introduced to enhance verifiability and self-calibration. This approach centered on the size (intensity) spectrum: again selecting gammalike images, but by what was termed the ellipsoidal window method; an alternative calibration using the charged cosmic-ray background; grouping events by size (intensity); adjusting the energy spectrum in simulations to match the observed size spectrum.

Both methods were applied to a large subset of the data used for our earlier published spectrum (Vacanti et al. 1991), taken between 1988 November and 1989 March. The first analysis used 52 pairs of "on" and "off" runs, each run usually of 28 minutes duration; the second analysis used 45 of these pairs, restricted to a smaller range of zenith angle $\sim 20°$. The first analysis was then also applied to 49 run pairs taken between 1995 January and 1996 March, when the optical efficiency had been improved by adding light concentrators to the phototubes and lowering electronic thresholds, and by recoating mirror facets. All analyses started by cleaning the images to remove signals not far above noise and then characterizing each image by its size (total signal) and the four image parameters, distance of centroid from direction of Crab Nebula, rms width and length of image, and orientation angle α (angle by which the image axis fails to point at the Crab Nebula). (See Reynolds et al. 1993 for more quantitative definitions.) As indicated above, the vast majority of images, in which these parameters did not fall within a selection window, were rejected as not being gamma-ray candidates.

2.1. *Selection of Gammalike Images*

Images of Cerenkov flashes are normally selected by shape and position—requiring the length, width, and distance of an image to lie between specified limits—and then by orientation, requiring α to be less than, say, 20°, this process of background rejection ensuring the greatest S/N for typical sources (Punch et al. 1991; Reynolds et al. 1993). However, in order to select gamma-ray showers efficiently over a wide range of energy, it is necessary to change these acceptance limits for showers of different energy, or, more practically, for different event sizes. The position of shower maximum moves deeper in the atmosphere by 2.3 radiation

lengths per decade increase of energy, and thus closer to the observer. Hence, the angular width and length of the shower image increase with the logarithm of the energy, or, in practical application, with the logarithm of shower size (image intensity). These limits or "cuts" in each parameter that effectively isolate the gamma-ray images cannot be derived directly from the data for many separate energy domains, as statistics are quite inadequate, so one must necessarily rely on simulations to determine these limits. Completely different Monte Carlo simulations were used in the two methods: this assured us of the physics of the relationship between light production and gamma-ray energy, as there was good agreement. Agreement of the predicted image dimensions with main features of the observations could also be checked directly near the median energy of the data. In fact, predicted mean image widths in gamma-ray events at energies near 1 TeV are found to be $\sim 0.^{\circ}01$ (i.e., 8%) smaller than those of real images; so there is some minor factor spreading the light—probably within the telescope—that has not yet been traced. Method 1 used a Monte Carlo simulation program developed by Mohanty (1995) from the KASCADE program of Kertzman & Sembroski (1994). Method 2 used the MOCCA92 program (Hillas 1995). In both of these, Cerenkov photons were followed over the wavelength range 185–685 nm, modeling atmospheric absorption, followed by detailed ray tracing through the telescope to locate which photomultiplier, if any, detected the photon, with realistic efficiency and pulse variance. Noise was added to the images to mimic the true observed sky noise, and the simulated images were cleaned and parameterized in the same manner as real images. The triggering characteristics of the electronics proved difficult to model exactly, and so the simulated spectra of flashes cannot be relied on close to threshold. Hence, one obtains the expected mean values and distributions of image parameters as a function of energy, and alternatively as a function of event size. (Although a particular assumed spectrum of energies is used for the latter determination, the result is very weakly dependent on the spectrum slope in the range of present interest.)

In the case of method 1, suitable limits or cuts in the values of distance, width, length, and α were determined for selecting gamma-ray events with $\approx 90\%$ efficiency. These limits were referred to as "extended Supercuts," and for showers detected at around 20° from the zenith, corresponding to the median of the Crab observations, the selection criteria thus derived were found to vary with event size as follows: $0.60 <$ distance < 1.0; $|\text{width} + 0.022 - 0.023 \ln(\text{size})| < 0.048$; $|\text{length} - 0.114 - 0.020 \ln(\text{size})| < 0.068$; $\alpha + 0.558 \ln(\text{size}) < 22.66$ (distance, length, width, and α in degrees; size in electronic ADC units, effectively units of 1.15 photoelectron).

Method 2 used what was intended to be a slightly more efficient (ellipsoidal) shape of selection window in parameter space: one whose boundary could also be defined conveniently by a simple mathematical prescription. Each recorded image is regarded as a point in four-dimensional parameter space (distance, width, length, α). Gamma-ray images cluster in a small region of this space, whereas background cosmic-ray images are widely spread (as illustrated, for instance, in Fig. 4 of Mohanty et al. 1998 or in Hillas & West 1991), so an event was accepted if the point lay within a suitably chosen sphere drawn around a center defined by the mean value of each parameter obtained from simulations. As there are more than three dimensions in this parameter space, this selection method has usually been referred to as the "hypersphere" selection method (Hillas & West 1991; West 1994), but we prefer the term "ellipsoidal window." The principle is that the distribution in parameter space, and hence the acceptance window, can be made approximately spherical by appropriate scaling and combination of the parameters, but this process is encapsulated by taking the Mahalonobis distance r of any point in parameter space from the cluster centroid, as follows. If p_1, p_2, p_3, p_4 are the values of the four parameters (distance, width, length, α) and simulations predict mean values of $\langle p_1 \rangle$, etc., then

$$d^2 = \sum_{i=1}^{4} \sum_{j=1}^{4} M_{ij}(p_i - \langle p_i \rangle)(p_j - \langle p_j \rangle) . \quad (1)$$

The matrix M_{ij}, which represents the metric in parameter space, is the inverse of the covariance matrix C_{ij}, where $C_{ij} = \sigma_{ij} = \langle p_i p_j \rangle - \langle p_i \rangle \langle p_j \rangle$. This matrix has to be calculated from a large sample of simulated images. Different centers and matrices were computed for each third of a decade of flash intensity, to allow for the gradual change in image shape with energy. Accepting images with distance $d < d_{\max}$, one has numbers n_{on} in the on-source run and n_{off} in the off-source run of equal duration. The on-source excess $(n_{\text{on}} - n_{\text{off}})$ obtained with window radii in the range $d^2_{\max} = 6$–10 was thus confirmed to be picking up 80%–90% of the limiting number of gamma rays that would be obtained in a large window. Also, checking that, as the window size $d_{\max}$ was reduced, the gamma-ray signal decreased in a manner close to that predicted by the simulations, checked that the simulations had put the selection window in the correct place in parameter space. In one older, less accurate simulation, for instance, it was seen that as the window radius was made small, the numbers of selected events disappeared very rapidly, as the predicted position of the center of the "gamma-ray cluster" was incorrect. Before any images were accepted for window selection, an initial hard cut in distance was imposed, as in method 1, but in method 2 the wider range of $0.5 <$ distance < 1.1 could be accepted, as the method of handling the size-energy relationship in the latter was more tolerant of the nonlinearities in this relationship that set in at distances greater than $1.^{\circ}0$.

2.2. *Derivation of Energies and Flux*

Method 1 assigned an estimated energy to each event, using a formula for ln (energy) of second order in ln (size) and distance, derived from the Monte Carlo simulations to give the best estimate of the primary energy, provided that distance lies within the range $0.^{\circ}6$–$1.^{\circ}0$. Because the size of an event varies highly nonlinearly with distance near $1.^{\circ}0$ (because of losses at the edge of the camera and also because impact points may then be beyond 125 m), the terms in this polynomial approximation would be very different for a different range of the fitted parameters, and it is not useful to quote the actual formula here. The simulations indicated that the rms error Δ in ln E obtained thus for individual images is 0.36. This energy conversion is of course at the heart of the spectrum determination, and the considerable scatter in the true energy of events with the same size and distance can introduce bias into the spectrum because the same size of event can be produced by upward fluctuations of lower energy showers or by downward fluctuations of

higher energy showers, and the steeply falling spectrum makes the former much more numerous. If this effect were not allowed for in calculating the effective collecting area, the flux would, in fact, be overestimated by a factor exp $\frac{1}{2}[\Delta(\gamma - 1)]^2 = 1.16$ in the present case, where γ (≈ 2.5) is the exponent of the differential energy spectrum.

The effective collection area is found by throwing simulated gamma-ray showers uniformly over an area extending to 250 m from the telescope[16] and applying all the same "cleaning" methods, selection criteria, and processing methods to the simulated images that were applied to the real images (but assuming that the triggering electronics switched on precisely when two of the inner 91 photomultipliers registered more than 50 ADC units). At each energy, the effective area is then $\tilde{A} = \pi(250\ \mathrm{m})^2 \times$ (the fraction of simulated showers that are accepted in a specific energy range). (In fact, this "fraction" can rise above 1.0 because of the upward energy fluctuations that arise in the analysis, as discussed above.) The collecting area thus obtained for the 1988–1989 season remains near 5.8×10^4 m^2 from 5 TeV down to 1 TeV, below which it falls off, dropping to 10% of this plateau at 320 GeV. The "spectrum threshold energy," at which the gamma-ray detection rate per TeV peaks (for a source with an output $dN/dE \propto E^{-2.5}$) is ~ 500 GeV. Without a software cut on size and on second largest photomultiplier tube signal, the response would have extended to lower energies.

For simulating the signal sizes in ADC units, the reflectivity of the mirror and the photoconversion efficiency of the photomultipliers, as a function of wavelength, were taken from figures supplied by the manufacturers, although a uniform degradation in reflectivity to 85% of the original level was estimated to have occurred, judging from the rate of loss of reflectivity during a year. Laboratory measurements (Kwok 1989), made on representative photomultipliers with appropriate voltage settings, were used to supply the conversion that one photoelectron produced an average pulse height of 1/1.15 ADC units (with all appropriate amplifiers and cable losses in operation).

Using method 1, the best power-law fit to the resulting spectrum for $0.5 < E < 5$ TeV in 1988–1989 was

$$J(E) = (3.41 \pm 0.25) \times 10^{-7} \times (E/1\ \mathrm{TeV})^{-2.38 \pm 0.10}\ \mathrm{m}^{-2}\ \mathrm{s}^{-1}\ \mathrm{TeV}^{-1}\ , \quad (2)$$

where only the statistical uncertainty is quoted. Points are plotted in Figure 1, with 1 σ statistical errors. The symbol $J(E)$ will denote the photon flux per unit interval of time, energy, and area.

A similar analysis of 1995–1996 data, with the cuts somewhat modified to allow for the slightly different characteristics of a modified photomultiplier array, having light-collecting cones to improve the efficiency, gave

$$J(E) = (3.12 \pm 0.40) \times 10^{-7} \times (E/1\ \mathrm{TeV})^{-2.57 \pm 0.12}\ \mathrm{m}^{-2}\ \mathrm{s}^{-1}\ \mathrm{TeV}^{-1}\ . \quad (3)$$

Turning now to method 2, the events were separated into different bands of size, and the ellipsoidal-window selection criteria were applied for each size band, resulting in the number of gamma-ray images seen in each band of size (intensity) during 20.76 hr of on-source observation. Rather than using an effective collecting area to make the step to photon flux, a library of simulated images was then consulted to find what numbers of gamma rays within different energy bands should be used in the simulation so as to result in this size spectrum being obtained when these triggering and selection criteria were employed. The result (for the season 1988–1989) could be written as

$$J(E) = (3.30 \pm 0.25) \times 10^{-7} \times (E/1\ \mathrm{TeV})^{-2.60 \pm 0.13}\ \mathrm{m}^{-2}\ \mathrm{s}^{-1}\ \mathrm{TeV}^{-1}\ . \quad (4)$$

The approach used in method 2 to model the threshold response of the voltage discriminators that triggered the recording system was less successful than that used in method 1, so the spectrum was not reliable below 0.8 TeV using this method. Hence, because of the smaller energy range fitted here, the exponent is not determined quite as accurately as in method 1. From the points plotted in Figure 1, it will be seen that the difference in exponents obtained by the two methods is not significant.

The spectrum of flash intensities seen off source due to cosmic-ray protons and nuclei was also predicted from the known fluxes of cosmic rays (represented by formulae fitted by A. M. Hillas to well-known data and given in Kaye & Laby 1995; see the Appendix of Mohanty et al. 1998, which corrects one error in the Kaye & Laby tabulation), and the comparison of this with observed off-source image spectra taken at the time was used to make a final adjustment of the assumed "gain" of the detector. Agreement could be obtained by replacing the average signal of 0.87 ADC units photoelectron^{-1} from Kwok's measurements by 0.75 (the figure adopted for the spectrum determination above), though this modest 13% adjustment to the a priori gain could reflect small errors in the assumed atmospheric transmission or mirror reflectivity, rather than a change in electronic gain. It serves as an overall test on the multiplicative effect of all these factors.

2.3. *Comments*

The direct simulation of size spectrum in Method 2 is an important check of the results obtained by assigning energies to all the events, because sharp nonlinearities in the energy-size relationship occur for showers at the outer boundary of the acceptance area and also when saturation occurs in the brightest pixels (at 3–4 TeV). It may be difficult to represent these effects by analytical formulae for energy, but they are fully taken into account in the direct simulations and hence in the simulated size spectrum. The alternative method of calibration, using cosmic-ray showers, is thought to provide reassurance that there is no important light loss mechanism related to variable contaminants of the atmosphere. Such sporadic effects were not expected, because the rate of observing background showers is remarkably stable on nights that appear clear to visual inspection.

We note here that the first attempt to derive spectra using extended Supercuts was reported by Lewis et al. (1993), but this resulted in a lower and more steeply falling flux from the Crab Nebula. We find that the main reasons for the differences on that occasion were the use of incorrect sensitive areas for the photomultipliers, the use of simulations for vertical rather than inclined showers, and the lesser

[16] This target area and the derived collecting area are defined in a plane passing through the mirror rim and normal to the direction in which the telescope is aimed.

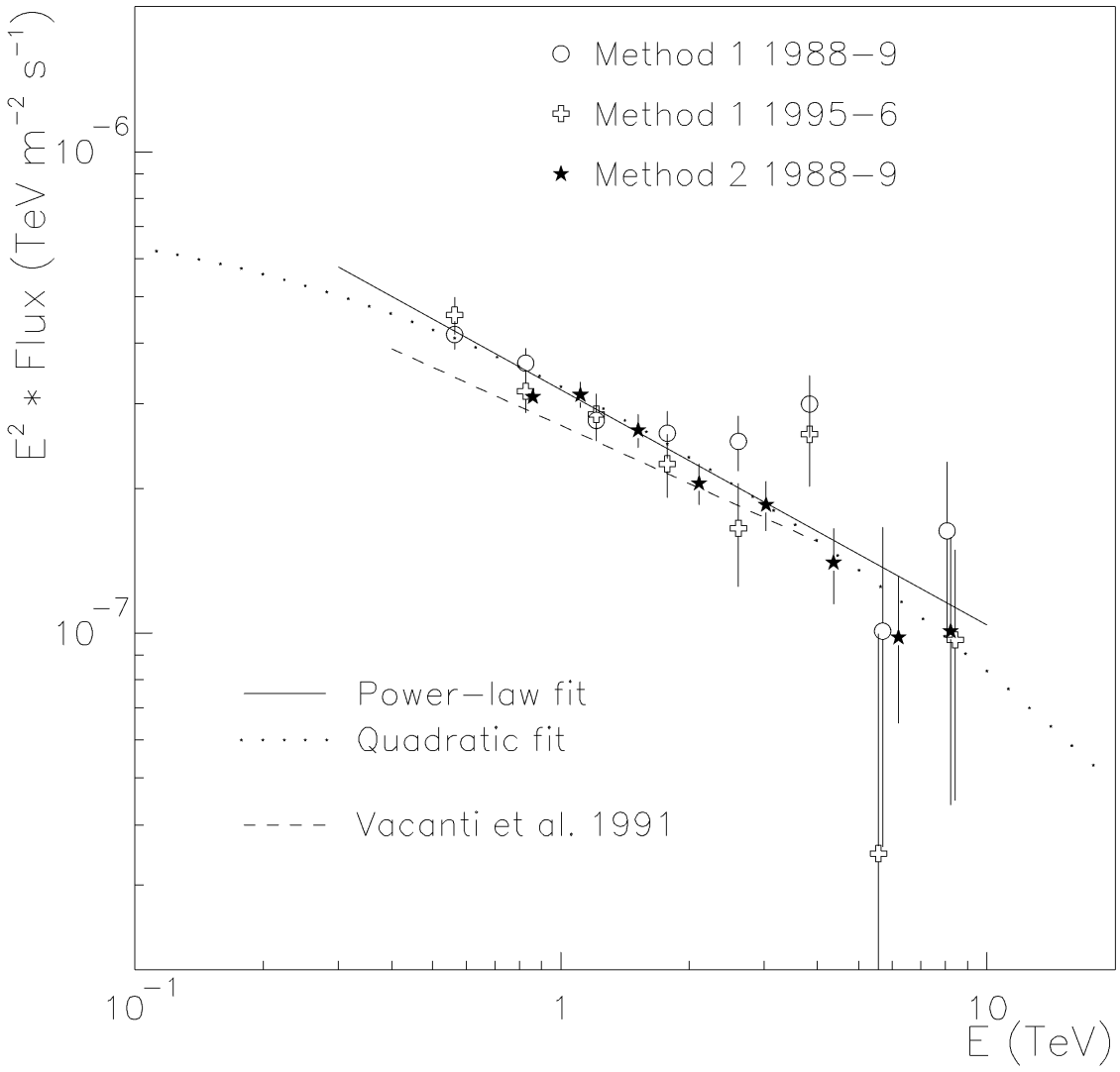

FIG. 1.—Spectrum from the two methods. *Solid line:* Simple power-law fit; *dotted line:* quadratic fit in log *E*. *Dashed line:* Our previous result (Vacanti et al. 1991).

robustness of the earlier analysis method to the use, then, of images of distance beyond 1°. These factors have now been corrected.

2.4. *The Spectra Obtained*

The three sets of results are plotted together in Figure 1 to show the degree of consistency, the error bars indicating 1 σ ranges, excluding systematic errors.

The three independent analyses could be represented by equations (2)–(4). Fitting a power-law spectrum to all the points shown in Figure 1 gives the following flux:

$$J = (3.20 \pm 0.17 \pm 0.6) \times 10^{-7} \times (E/1\ \mathrm{TeV})^{-2.49 \pm 0.06 \pm 0.04}\ \mathrm{m^{-2}\ s^{-1}\ TeV^{-1}}\ . \quad (5)$$

The quoted uncertainties reflect, first, statistical errors and second, systematic uncertainties estimated in Mohanty et al. (1998). In equation (5) the statistical uncertainties have been determined from the behavior of χ^2. With 1 TeV used as the reference energy in the formula, the correlation between uncertainties in the intensity constant and the exponent is small.

If the spectrum (eq. [5]) is extended to much higher energies, the corresponding integral flux above 1 TeV is

$$I(>1\ \mathrm{TeV}) = (2.1 \pm 0.2 \pm 0.3) \times 10^{-7}\ \mathrm{m^{-2}\ s^{-1}}\ . \quad (6)$$

However, if the spectrum (5) is extended back to the GeV energy range, it comes more than an order of magnitude above the flux obtained from the EGRET experiment (de Jager et al. 1996),[17] so the spectrum must clearly be curved on a plot of log J versus log E, and the magnitude of the spectral exponent must be increasing as energy increases. As an aid to linking our data to fluxes obtained in other experiments, we have therefore also fitted a parabolic curve in log J versus log E, using the single additional constraint that the spectrum will join on to the high-energy points of the EGRET experiment by yielding an intensity 0.10 $\mathrm{m^{-2}\ s^{-1}\ TeV^{-1}}$ at 2 GeV—a single representative point, so as to constrain only the intensity and not the slope here. A fit to our data points minimizing χ^2 and using the EGRET constraint to determine the curvature parameter is obtained

[17] Preferred to Nolan et al. (1993), as that run included data contaminated by a solar flare.

with –

$$\log_{10} J = -6.488 - 2.44 \log_{10} E - 0.151 (\log_{10} E)^2 \quad (7)$$

(J in $m^{-2}\ s^{-1}\ TeV^{-1}$, E in TeV)—shown as a dotted line in Figure 1. This may alternatively be written as

$$J = (3.25 \pm 0.14) \times 10^{-7} E^{-2.44 \pm 0.06 - 0.151 \log_{10} E}\ m^{-2}\ s^{-1}\ TeV^{-1}\ . \quad (8)$$

The quadratic form is also quite close to the shape expected theoretically at higher energies, as discussed in § 3. The systematic uncertainty in flux at 1 TeV will again be about 21%. The uncertainty in the exponent 2.44 is only weakly correlated with the uncertainty in the amplitude, 3.25. The curvature parameter should always be chosen, for given values of the other parameters, to yield the 2 GeV flux correctly. The integral of equation (8) is given in Appendix A, and it would yield an integral flux above 1.0 TeV of $2.14 \times 10^{-7}\ m^{-2}\ s^{-1}$.

In order to compare our results to those of most other workers, we have to convert to integral fluxes, and the result is affected by the choice of either equation (5) or (8) to estimate the total flux above the highest energy in our measurements.

For each of our methods, the integral flux above the highest data point is obtained by integrating equation (8), and then the integral increment to each successive point at lower energy is obtained by using simple power-law interpolations to join successive data points. Figure 2 shows the results as filled points. If, instead, equation (5) is used to estimate the integral flux above the highest energy observed, all points are raised (*open symbols*). Dotted lines show the integrals of equations (5) and (8), though the simple power law is not shown below 1.5 TeV. Intensities reported recently by several other workers are also shown, together with several upper limits quoted at higher energies (mostly quoted at the Rome International Cosmic-Ray Conference in 1995). The upper limits found by the CASA-MIA array above 100 TeV (Borione et al. 1997) are seen to be inconsistent with the straight power-law extrapolation, but no data contradict the preferred quadratic form. Our flux matches well other measurements above 7 TeV—for instance, the most recent results from the CANGAROO telescope (Tanimori et al. 1998)—but appears slightly higher than

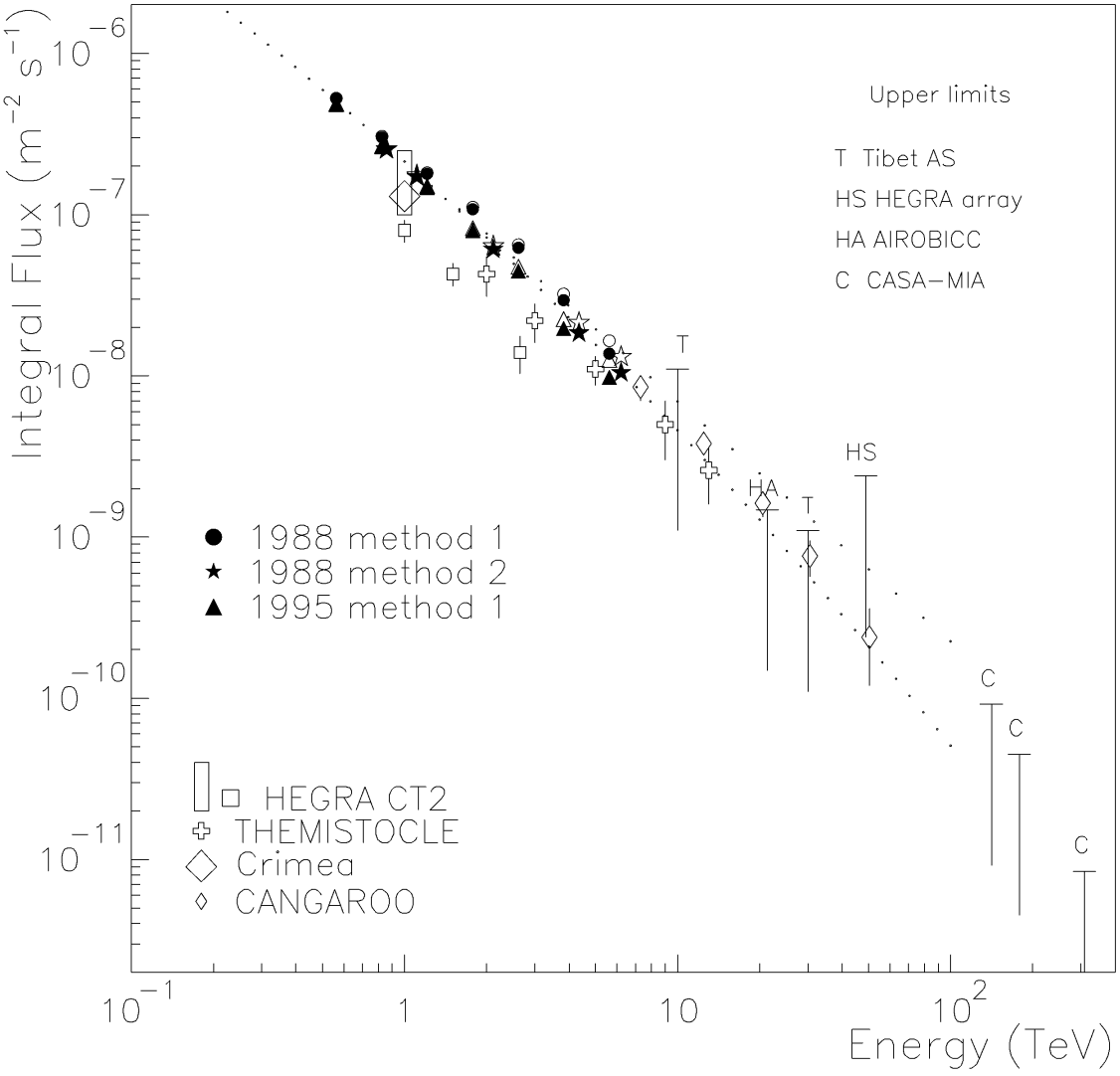

FIG. 2.—Integral flux of photons from Crab Nebula obtained by various workers. *Upper dotted line:* Power-law fit to the Whipple points [i.e., log (flux) is linear in log E]; *lower dotted line:* quadratic fit in log E.

other reported fluxes near 1–2 TeV, from the THEMISTOCLE and Crimean installations (THEMISTOCLE collaboration 1995; Stepanian 1995). The HEGRA CT2 flux at 1 TeV (Petry et al. 1996) is consistent with our value, being slightly higher than earlier estimates (Konopelko et al. 1996). We have not made a quadratic fit incorporating other TeV data, as this would require a close examination of their discrepancies; however, we note that fitting also to the CANGAROO points, that seem well normalized to ours and that suggest the flux may be a little higher than our fit above 10 TeV (though well below the power-law extrapolation) would have made a negligible difference to the derived parameters. The less simple curve of theory (see Fig. 6) may, however, be a better fit.

3. IMPLICATIONS OF THE RESULTS

The radiation from the Crab Nebula is dominated by synchrotron emission from radio frequencies right through to 10^8 eV gamma rays, near where the synchrotron flux ends sharply (Fig. 4). To produce this radiation, there must be relativistic electrons or positrons in the nebula with energies extending to somewhat above 10^{15} eV, and these are capable of producing GeV–TeV photons by inverse Compton scattering of the ambient photons in the nebula, which are primarily the synchrotron photons, but also infrared emission from dust, together with the 2.7 K primeval radiation. To produce gamma rays above 200 GeV, where the scattering occurs in the Klein-Nishina rather than in the Thomson scattering regime, it turns out that the electrons must have energies $E \approx E_\gamma \times 5E_{\gamma,\mathrm{TeV}}^{-0.12}$ (i.e., about 2–30 TeV for our observations), and the relevant target photons would mostly have energies 5×10^{-3}–0.3 eV, these figures coming from calculations described below, although they are not very model dependent. The first discussions of this process were given by Gould (1965) and Rieke & Weekes (1969), and then with the assumption that the mag-

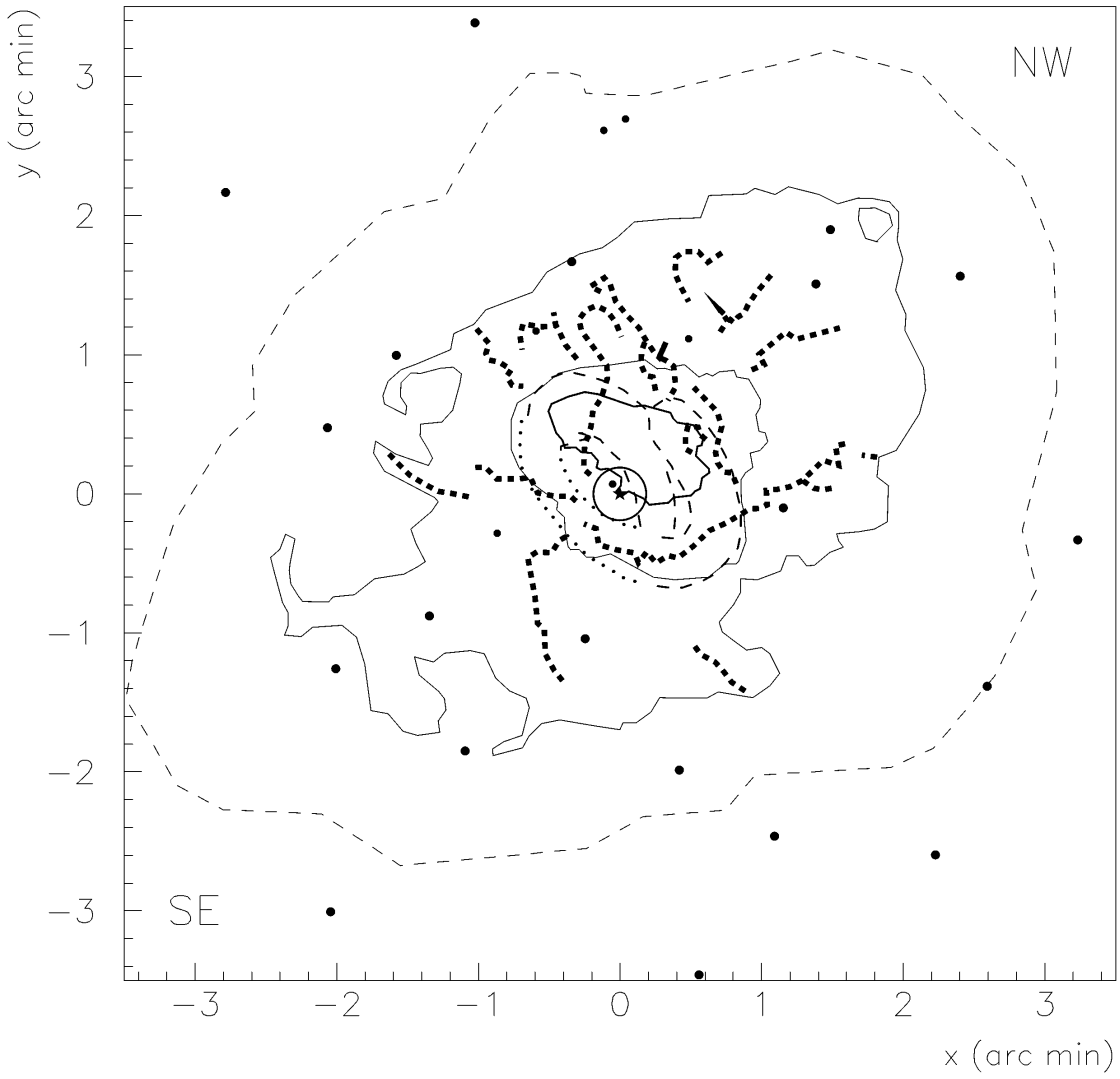

FIG. 3.—Regions of emission in the Crab Nebula (y is the declination axis). A small region around the pulsar (*star*) contains the relativistic wind, terminating sharply at a shock where a power-law spectrum of particles is supposedly generated. *Outer dashed line:* Approximate outer boundary of radio emission. Three solid-line contours inside this, enclosing successively smaller regions, show (*a*) the contour of 20 cm radio emission at 35% of the central intensity, (*b*) the contour of 40% of peak intensity of X-ray emission, and (*c*) 70% of peak X-ray emission. The X-ray emission region has been interpreted as a distorted torus, sketched roughly (from Fig. 4*c* of Hester et al. 1995) by dashed lines on the northwest side of the pulsar and by dotted lines to the southwest, where the emission is clearly fainter. The optical continuum is extended somewhat like the radio contour (*a*), but a local brightening occurs roughly where the X-rays are brightest. The TeV emission is expected to follow X-ray emission fairly closely, though the inner edge of the torus will be brighter. *Thick dashed lines:* Positions of the more prominent filaments of thermal gas. The dust may be concentrated in the same region, but this is not known. (Scale: At a distance of 2 kpc, 1′ represents 0.58 pc.)

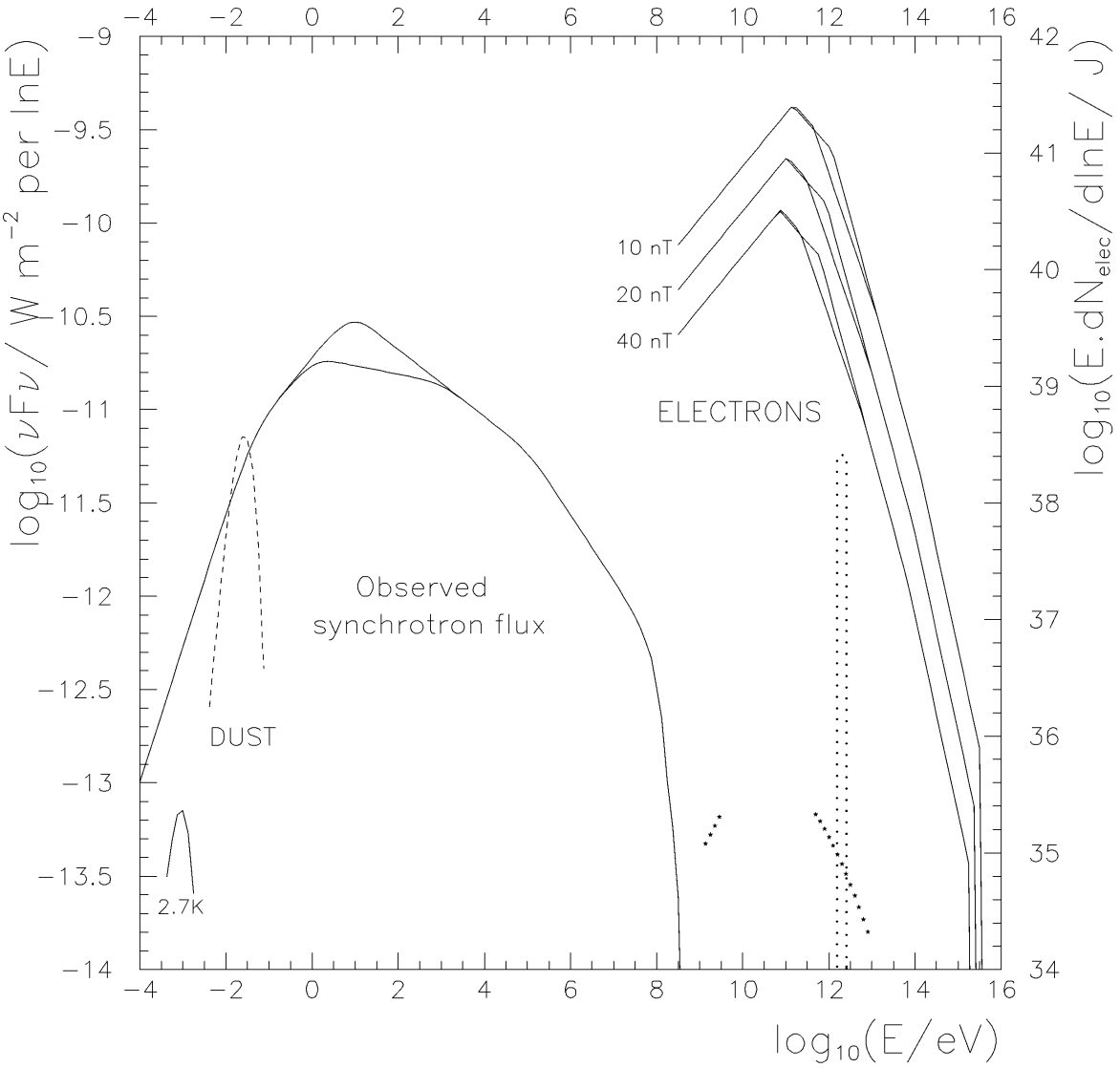

FIG. 4.—Observed flux of synchrotron photons from Crab Nebula (power per unit area per unit range of ln E) and deduced energy spectrum of electrons in nebula (energy content per unit range of ln E), for various assumed magnetic field strengths. *Dashed lines:* Spectra of thermal radiations, scaled to show photon density relative to synchrotron photon density in main emitting region. *Heavier dotted line:* For comparison, the nonsynchrotron component where known between 10^9 and 10^{13} eV, which is the subject of this investigation. *Lightly dotted line:* Estimated additional electrons in the relativistic wind, before the termination shock (though the energy range, 0.5 in ln E, is chosen arbitrarily).

netic field strength falls with distance from the center, by Grindlay & Hoffman (1971) and Stepanian (1980, 1990), whilst excellent recent discussions have been published by de Jager & Harding (1992), followed by Aharonian & Atoyan (1995), Atoyan & Aharonian (1996), and de Jager et al. (1996). Despite a considerable spread of predicted intensities in the earlier papers, these works have shown that such a scattering process gives a very reasonable description of the intensity and spectral shape in the TeV region, though perhaps predicting too low a GeV flux.

Before comparing our observations to the specific predictions of these recent models, it seems most appropriate in this paper to stay as close as possible to the observational results and the simplest inferences that may be drawn from these. Hence we shall present the whole observed spectrum of the Crab Nebula up to 10^8 eV and then deduce as directly as possible the energy spectrum of the relativistic electrons that would result in this synchrotron spectrum, if a specific strength of magnetic field is assumed in the important region of the nebula. Thus having the energy spectrum of the relativistic electrons, which scatter the infrared photons, the flux of the resulting TeV photons can be predicted. This is essentially the approach followed by most of the early discussions, such as by Rieke & Weekes, but we now have the benefit of more complete measurements of the synchrotron spectrum of the Crab Nebula, and modern computers make it simple to represent the radiation and scattering cross sections exactly. The greatest uncertainty arises in turning the known power of the source in the infrared domain into a photon density, in order to calculate the scattering rate, as this transformation involves the spatial distribution of the emission within the nebula, which is not known in detail, in particular for the dust component.

Underlying the recent theoretical studies quoted above is the following interpretation of the structure of the nebula, which is depicted in Figure 3. The magnetic energy emerging from the spinning pulsar is almost entirely converted to ordered outward motion of monoenergetic relativistic

charged particles (mainly electrons and positrons with Lorentz factor 10^6–10^7), concentrated toward the pulsar's equatorial plane, so that when this ordered motion ends at a termination shock, about 0.1 pc (0′.2) from the pulsar, the field strength may be as low as ~ 4 nT and entirely transverse. (See, for instance, Rees & Gunn 1974; Coroniti & Kennel 1985; for different models see Kundt and Krotschek 1980; Michel 1985.) From this ordered flow there would be almost no synchrotron radiation. At the shock the electron momenta are randomized and converted to a power-law spectrum (though the mechanism may be an unusual one; Arons 1995 and references therein) and the magnetic field enhanced. From here the outflow speed drops smoothly, with the magnetic field hence being further compressed and enhanced. Kennel & Coroniti (1984a, 1984b) have modeled a simple hydrodynamic motion of the plasma of the nebula that carries and compresses the magnetic field from the pulsar wind. According to them the magnetic field strength should first increase linearly with distance, but should then change little beyond $\sim$0′.6–1′.2 from the pulsar. The most energetic electrons would radiate away their energy very quickly, even in the lower field region close to the shock, whereas the electrons below TeV energies could convect and diffuse well into the constant-field main region of the nebula. Unlike the simpler approach adopted here, the papers by de Jager & Harding (1992) and by Atoyan & Aharonian attempt to allow explicitly for such a pattern of spatial variation of magnetic field and energy loss by electrons, in order to deduce the electron spectra at various regions of the nebula, and from that to calculate the inverse Compton emission, although a comprehensive model is hampered by assumptions of spherical symmetry and by lack of agreement about the mode of generation of the main bulk of sub-TeV electrons.

For magnetic field strengths of ~ 16 nT, which are required, the electrons of several TeV generate synchrotron radiation of around 0.4 keV, and so one can see where in the nebula the TeV gamma rays originate—from the *Einstein Observatory* X-ray pictures of Harnden & Seward (1984) and later *ROSAT* pictures (see Hester et al. 1995). Figure 3 shows the regions of the Crab Nebula from which the main emission is observed in 0.3–4 keV X-rays (mapping ~ 6 TeV electrons), 20 cm radio waves, (Wilson, Samarasinha, & Hogg 1985; mapping 1 GeV electrons), and the optical filaments, the most likely but not certain tracer of the dust. Thus the electrons of interest to us are found in a well-defined region, asymmetrically placed within the nebula, centered at a projected distance about 0′.4 from the pulsar. Our observations relate principally to the magnetic field and photon density in this part of the nebula. The photons that are being upscattered are mainly far-infrared, and include synchrotron photons—which almost certainly have a distribution similar to that of the radio photons—and also emission from dust, which seems to be associated with the optical filaments, but could possibly be found further out. The appearance of the Crab Nebula shown in Figure 3 illustrates the general view that the synchrotron radiation issues from two populations of electrons: first, a widely extended population of energies up to ~ 100 GeV, generated over the whole lifetime of the nebula, responsible for the radio to infrared photons; second, electrons from $\sim 10^{12}$ eV upward, concentrated in a torus sketched by dashed lines in Figure 3, having been accelerated in the shock terminating the pulsar wind that emerges mainly near the equatorial zone of the pulsar (Aschenbach & Brinkmann 1975; Hester et al. 1995). The alignment of the extended population of electrons suggests that these may issue from the axial regions of the pulsar. *Hubble Space Telescope* pictures (Hester et al. 1995) show features suggesting ejection of particles near the pulsar axis.

We come now to the observed wideband spectrum of the Crab Nebula, shown in Figure 4, where it is represented by power-law segments in successive domains of photon energy, with a rapid fall above 100 MeV. The soft X-ray region of the spectrum is somewhat uncertain, because the well-defined $E^{-2.18}$ number spectrum of the harder nebular X-rays (Bartlett et al. 1994) does not join neatly to the optical spectrum (corrected for considerable interstellar extinction), and a plausible band of uncertainty is shown in Figure 4 for the synchrotron spectrum in this heavily obscured region. Indeed, the multipart spectrum in this region seems to require the presence of more than one population of radiating electrons, such as the extended population of electrons responsible for photons below about 1 eV and the more recently accelerated electrons in the torus described above. (Aharonian & Atoyan have worked with such a two-component spectral model.) The figures used to represent the synchrotron spectrum are given in Appendix B. The spectrum above 0.5 MeV may exhibit a dip that is not included in this description (see de Jager et al. 1996), but this has no bearing on the generation of scattered gamma rays below 10 TeV.

Assuming some specific magnetic field strength in the region of emission, and a distance of 2 kpc to the nebula (though not precisely known; Trimble 1968), the number spectrum of electrons in the nebula can be deduced (Appendix B), as shown also in Figure 4, where the three curves refer to spectra for assumed field strengths of 10, 20, and 40 nT. The spectrum of emitted inverse Compton–scattered photons can be deduced from the electron spectrum once one has converted the detected photon spectrum of Figure 4 into a spectrum of photon densities. If these target photons are produced with a volume emissivity varying as $e^{-(r/\sigma)^2/2}$ at a distance r from the center, and with a total photon production rate of S, the photon density at the center is $S/4\pi c\sigma^2$. If the electrons have a density that also falls off as a Gaussian, with a scale length ρ, i.e., as $e^{-(r/\rho)^2/2}$, the average density of photons seen by the electrons that are interacting with them is reduced to $S/4\pi c(\sigma^2 + \rho^2)$. Thus the flux of inverse Compton photons is very sensitive to σ and is generally less sensitive to the smaller ρ.

As notably different figures are quoted in the literature for the size of the photon source at different frequencies, the figures used here were measured from the maps of the Crab Nebula shown by Wilson (1972). The 5 GHz intensities were plotted out along the major and minor axes of the Nebula, running through the pulsar's position, and also along lines bisecting these directions. Averaging over these eight directions away from the pulsar, the brightness at a projected angular distance θ was found to be well described by a Gaussian curve $e^{-(\theta/\chi)^2/2}$, with $\chi = 1'.35$, although this average disguises the fact that the major axis is perhaps 60% longer than the minor axis. No change in scale has been detected to at least 250 GHz, and it seems natural to suppose that the size χ of the source remains constant up to a frequency near 10^{13} Hz, as the spectrum steepens at this point, indicating that losses over the lifetime of the nebula

are unimportant at lower frequencies than this. Wilson also displays the optical map of Woltjer (1957) in a similar format, and this was measured in a similar way, but about an offset center 0.′3 from the pulsar in a northwest direction, where there is a narrow intensity ridge containing 0.9% of the emission (coinciding approximately with the bright part of the torus), superposed on the broader distribution, which is again close to a Gaussian, with $\chi = 0.'88$. In the case of such a Gaussian pattern with emissivity varying with three-dimensional spatial distance r as $e^{-(r/\sigma)^2/2}$, the projected brightness also varies as $e^{-(r_{xy}/\sigma)^2/2}$, where r_{xy} is the two-dimensional projected radial distance, so σ can be derived directly from the brightness maps: $\sigma = D \tan \chi$, where D is the distance to the Crab Nebula (assumed to be 2 kpc, but canceling from the final predicted gamma-ray flux). Measuring the Harnden & Seward (1984) X-ray contour map in the same way, again from the same displaced center, gave $\chi = 0.'66$. In order to interpolate source sizes at other photon energies ϵ, it was assumed that arctan $(\sigma/D) = 1.'35$ for $\epsilon < 0.02$ eV and arctan $(\sigma/D) = 0.16 + 1.19(\epsilon/0.02\ \mathrm{eV})^{-0.09}$ arcmin for all higher photon energies. This form is guided crudely by expectations from a convection-diffusion model (Aschenbach & Brinkmann 1975; de Jager & Harding 1992), and it gives sizes very similar to those assumed by de Jager & Harding for 10^{-2} to 10^3 eV, though below 10^{-2} eV their size is larger (implying lower photon densities).

As a constant magnetic field is assumed, the scale distance ρ for the electrons was taken equal to the scale σ of the synchrotron source for the photons of the energy that would be emitted as synchrotron radiation.[18] Hence, arctan (ρ/D) is taken as $1.'35$ for electron energies E below 34 GeV and as $0.16 + 1.2(E/34\mathrm{GeV})^{-0.17}$ arc min above 34 GeV. This scale size for electrons only plays a significant role at the lowest energies (having the effect of reducing the rate of generation of GeV scattered photons), the more uncertain scale size of the electrons of several TeV being much less than that of the photons they scatter and so not contributing much to the sum $(\sigma^2 + \rho^2)$. In the case of the infrared photons emitted by dust, the scale size is not directly known. Assuming it to be related to the thermal filaments, arctan (σ/D) was estimated roughly as $1.'3$. On this basis, scattering of the thermal photons from dust was responsible for $\sim$25% of the TeV flux. Although it is possible that the dust formed farther out, with the result that the thermal photon density would be reduced, this is less likely, as there seems to be remarkably little evidence of supernova ejecta at greater distances. In any case, it has to be admitted that spherical symmetry is a poor approximation both for the low-energy photon source and for the X-ray source, and a more accurate description of the form of the particle and photon distributions is probably not justified in this discussion. The offset center for the Gaussian distributions corresponds to the peak brightness of a very asymmetrical torus. It is possible that the torus could be described more explicitly in the expressions for photon and electron densities, provided that the large azimuthal brightness asymmetry arose from beaming of radiation from a high-speed outward flow—a Compton-Getting effect—although the outflow speed here would have to be larger than that anticipated in a Kennel-Coroniti model.

Figure 5 shows the inverse Compton spectra that are hence derived from a simulation of the exact Klein-Nishina differential scattering cross sections and the electron and photon spectra presented above, assuming that the electron and ambient photon momenta are isotropic overall, the method being outlined in Appendix B. The results are shown for three assumed field strengths of 10, 16, and 40 nT (100–400 μG), and in each case the stippled area represents the uncertainty arising from the ill-defined UV–to–soft X-ray region of the observed synchrotron spectrum. For this purpose it is assumed that if there is any spatial variation in the magnetic field strength, it does not materially affect the spectral shape. Our data are shown, as in Figure 1, as well as data from EGRET (de Jager et al. 1996) and CANGAROO (Tanimori et al. 1998). Note that the three EGRET points of lowest energy lie in the tail of the synchrotron spectrum. Unfortunately, many other TeV observers have quoted integral fluxes. The observed flux of $(3.2 \pm 0.7) \times 10^{-7}\ \mathrm{TeV}^{-1}\ \mathrm{m}^{-2}\ \mathrm{s}^{-1}$ at 1 TeV corresponds to a magnetic field strength of 15 ± 1 nT in the region occupied by the TeV electrons, at an apparent distance of $\sim$0.4 pc from the pulsar, in the torus, if one takes the lower bound of the assumed synchrotron flux in the heavily obscured region. Alternatively, with the upper bound of the synchrotron flux and a field of 17 ± 1 nT fits this flux. This is the principal deduction from our observations. The GeV photon flux observed by EGRET is subject to large errors, and it could be consistent with magnetic field strengths 13–20 nT in the region occupied by 200–300 GeV electrons. Although the deduced number of relativistic electrons in the nebula scales in proportion to the square of its assumed distance, the assumed photon density in the source is independent of distance, and so the predicted gamma-ray flux in Figure 5 is independent of this distance.

Above 10 TeV, the CANGAROO points would be explained better by a somewhat lower magnetic field strength, perhaps around 10–12 nT, near 40 TeV. This will be taken up below, in connection with hydrodynamic models.

It is of great interest to compare the deduced magnetic field strength at 0.4 pc from the pulsar to that further out, affecting the extended population of electrons. The latter is not so well measured, however. First, it can be estimated, as by Marsden et al. (1984), from the position of a clean break in the infrared spectrum, which they placed at 10^{13} Hz. Attributing this spectral steepening to radiation losses during the $\sim$940 yr life of the Crab Nebula, application of Kardashev's (1962) formula $\nu_{\mathrm{break}} \approx 340 B^{-3} t_{\mathrm{yr}}^{-2}$ MHz (with B in gauss, t being the age of the nebula) gives $B = 34$ nT (although Marsden et al. quoted 30 nT). However, this formula was given by Kardashev as a "rough estimate," and both an approximate analytical treatment and a more accurate numerical integration show that where the spectrum is as hard as in this object, the break point is somewhat displaced to higher frequency. As discussed briefly in Appendix C, a value $B \sim 60$ nT is suggested. Because we do not know the detailed history of the nebula, this cannot be precise, although it is not easy to reproduce a clean break with a change of 0.5 in the exponent with a much smaller field. Second, it has been widely assumed that in the main part of the nebula the energy of the plasma material has become small, and the magnetic energy is equal to the

[18] To estimate the energy of emitted synchrotron photons corresponding to a particular electron energy, the magnetic field was taken as 32 nT for the radio-frequency synchrotron component, scaling down through 15 nT at X-ray energies, though the results depend very weakly on this.

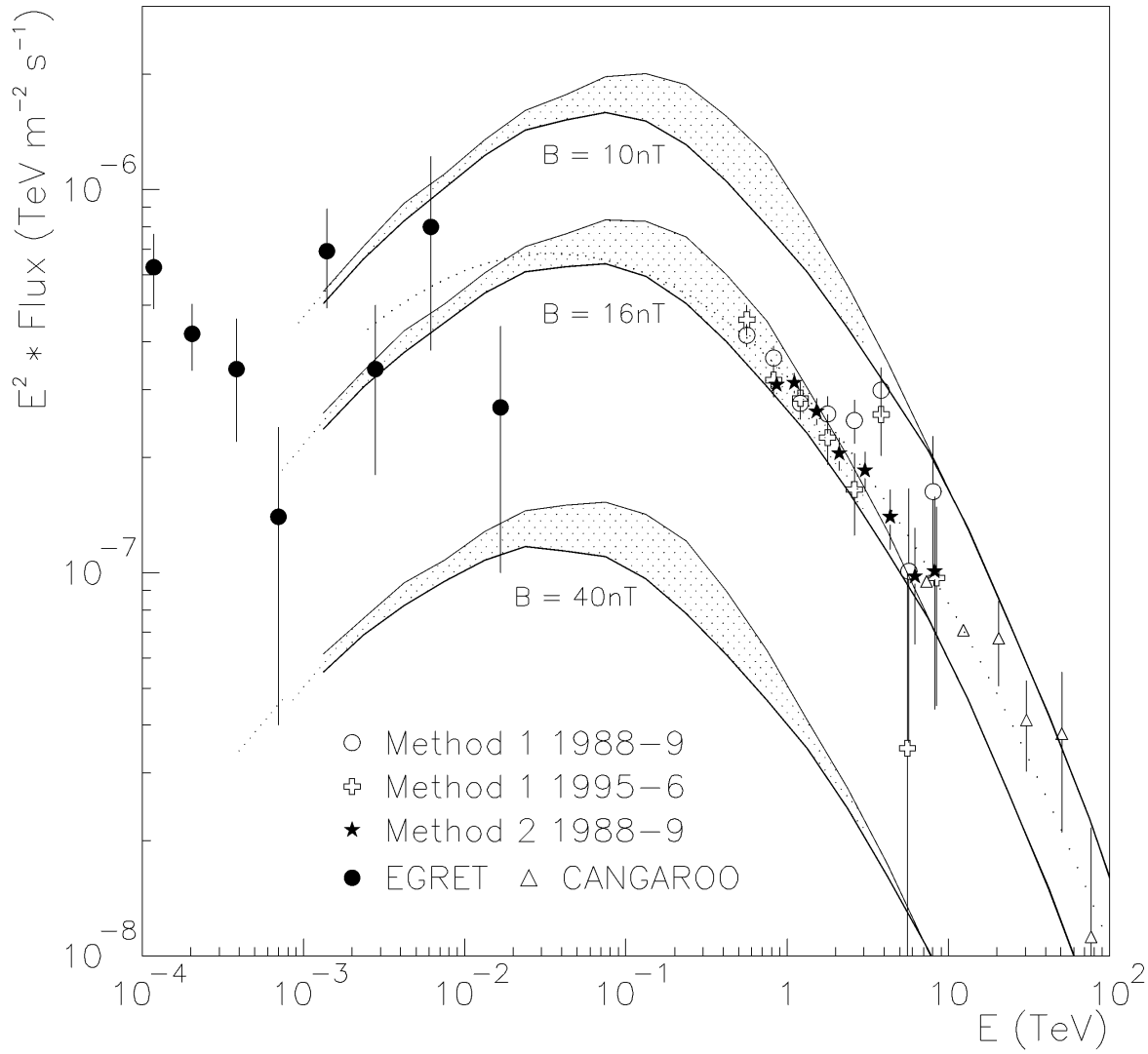

FIG. 5.—TeV spectra from the 1988–1989 and 1995–1996 data sets using the two analysis methods, compared to spectrum points from the EGRET and CANGAROO experiments, and with the predicted inverse Compton spectrum, the latter for three alternative field strengths as shown. *Dotted curve:* Parabolic fit in log E from Fig. 1.

energy in relativistic particles. To explain the radio luminosity, assuming such an equipartition, Wilson et al. (1985) estimated the field in the main part of the nebula as 41 nT, but they assumed that there was an appreciable energy carried by relativistic protons as well as electrons. The proton numbers may be small in the Crab Nebula, though, which would reduce the estimate of B to $\sim$33 nT. ($B_{\rm equipartition} \propto M^{0.3}$ for a given radio power, where M is the ratio of magnetic energy to energy in relativistic electrons, for a source with the radio spectral exponent as in the Crab Nebula.) Figures of 50 nT have also been quoted previously. In general, one might estimate equipartition field strengths ranging from 33 nT if there were very few relativistic protons present to 60 nT if the protons carried 10 times as much energy as the electrons (though the latter would be expected to give unacceptable acceleration to the expansion). Such field strengths are much larger than the strengths deduced in the X-ray–emitting region, and hence the assumption of equipartition between magnetic field energy and energy of relativistic particles may be questionable. Thus, the field in the main volume of the nebula is quite uncertain.

If the magnetic field in the nebula from the torus outward were roughly constant at 15–20 nT, and thus below the equipartition strength, all the data from 1 GeV to 8 TeV could be accounted for by inverse Compton scattering. Other contributions to the energetic gamma-ray flux should be small: the flux of sub-TeV photons due to electrons in the relativistic pulsar wind (typically $\approx$1 TeV) that scatter infrared photons is generally less than 1% of the observed intensity. Bremsstrahlung by the electrons has been ignored: Aharonian & Atoyan (1995) show that it should add a few percent to the fluxes in the GeV domain.

This discussion concerns what can be deduced about the Crab Nebula, from gamma-ray observations, without a specific model of hydrodynamic flow, and so it is complementary to the treatments of Atoyan & Aharonian (1996) and de Jager & Harding (1992), whose predictions are shown in Figure 6 for comparison with Figure 5. The curves marked "A.A" are from Atoyan & Aharonian, for three values of the mean magnetic field for the nebula. This mean is also the field strength at $\sim$0.4 pc from the center, and hence directly comparable with the field values quoted in Figure 5. The curves marked "deJ-H" are from de Jager et al. (1996),

and σ denotes the ratio of magnetic energy to total (mainly kinetic) energy in the pulsar wind. The data points and fit are the same as in Figure 5. These curves are not greatly different in shape from our predicted gamma-ray spectra; the calculations of Atoyan & Aharonian taken in conjunction with our data also indicate a magnetic field strength around 16 nT in the region where TeV gamma rays are produced. The more elaborate model in fact gives predictions surprisingly close to those obtained assuming a constant magnetic field, except that our predicted flux falls more steeply at the highest energies. Above 10 TeV, the data favor these hydrodynamical models (e.g., "A.A" $\sim$ 16 nT). This difference is to be expected, as the most energetic electrons must never move far from the shock before radiating away their energy: hence, they reside in a low-field region, and the electron numbers here would be higher than deduced when a constant 16 nT field is assumed (see Fig. 4). De Jager et al. (1996) deduced a field strength of $\sim$30 nT for the region of the torus, in contrast to a much lower field elsewhere. With our new observed spectrum, this would be reduced to about 24 nT, still $\sim$50% above our figure. These authors state that the GeV inverse Compton flux is related to electrons in the large-scale radio nebula, but the present calculations indicate that electrons of $\sim$200 GeV are involved, and that one could not use inverse Compton scattering to probe the outer nebula, as the resulting photons would be of energies well below 1 GeV and would be obscured by the synchrotron flux.

Aharonian & Atoyan have commented at length on an apparent deficit of GeV photons in their inverse Compton calculations, and they have suggested that another source is required, possibly bremsstrahlung from dense regions of gas. However, the EGRET flux measurements have large uncertainties. We see from Figure 5 that this problem may not arise if the magnetic field strength does not rise at distances just beyond the region of soft X-ray synchrotron emission. However, it should be borne in mind that the spatial structure of the Crab Nebula is much more asymmetrical than assumed in all the calculations, and this will be reflected to some extent in local densities of photons, which determine scattering rates. Small-scale structure has also been ignored. The *Hubble Space Telescope*'s high-resolution pictures of the Crab Nebula (Hester et al. 1995) suggest the synchrotron emission has a fibrous rather than

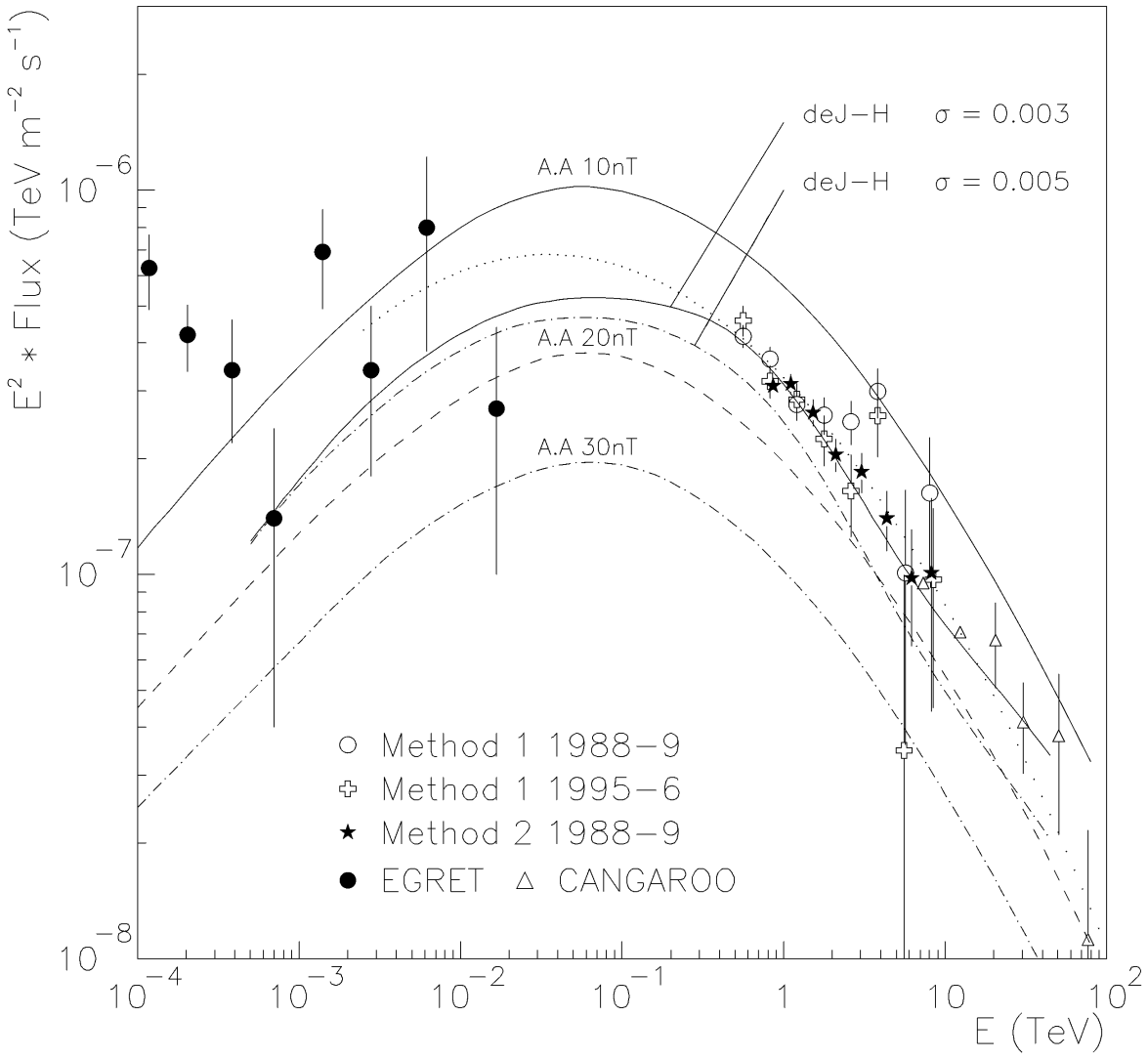

FIG. 6.—Predicted inverse Compton spectrum according to other workers, compared to our observed spectra and EGRET and CANGAROO spectra, the data points beng the same as in Fig. 5. "A.A" refers to Atoyan & Aharonian (1996) and "deJ-H" to de Jager & Harding (1992).

a smooth structure. However, even if the electron density is enhanced in corresponding platelike or thick ropelike strucures, the rate of production of TeV gamma rays would not be much changed.

Kwok, Cheng, & Lau (1991) have suggested an alternative origin for TeV gamma rays, proposing that unpulsed electron or positron beams streaming from an outer vacuum gap above the pulsar pole will generate photons of ~ 10 TeV, and that these can generate a cascade of secondary photons through the TeV to GeV domain, roughly matching the observed spectrum near 1 TeV. Within the uncertainties of the parameters, the spectrum might be quite similar to that discussed above, and so one could not rule out the possibility that we see a mixture of these two gamma-ray populations, provided that the magnetic field in the nebula is much stronger than 20 nT, so as to leave room for a component unexplained by the present inverse Compton process. However, if the pulsar component is significant, the spectrum will not continue smoothly above ~ 10 TeV, but will have a peak followed by a sharp drop. The CANGAROO data (Tanimori et al. 1998) do not appear to support this (see Fig. 6).

4. CONCLUSIONS

Fluxes previously quoted for the gamma radiation from the Crab Nebula have covered a range far outside the quoted uncertainties. We have thus found it necessary to check all parts of the process of selecting gammalike events, converting detector signals to photon energy, and deriving effective collecting areas. Using approaches that differ at several points and some quite different data sets, we get agreement on the fluxes to within 10%. The differential spectrum of gamma rays in the TeV region may be represented by the equation (5), to which we add the systematic uncertainties:

$$J = (3.20 \pm 0.17 \pm 0.6) \times 10^{-7} \times (E/1\ \mathrm{TeV})^{-2.49 \pm 0.06 \pm 0.04}\ \mathrm{m^{-2}\ s^{-1}\ TeV^{-1}}\ . \quad (9)$$

However, this form is clearly inadequate over much more than a decade of energy, as its downward extension would pass far above the flux measured in the GeV region by the EGRET experiment (de Jager et al. 1996). A good fit to our data that also agrees with the EGRET flux near 2 GeV is provided by a formula in which log J is quadratic in log E. This may be written (eq. [8], with added systematic uncertainties) as follows:

$$J = (3.25 \pm 0.14 \pm 0.6) \times 10^{-7} \times E^{-2.44 \pm 0.06 \pm 0.04 - 0.151 \log_{10} E}\ \mathrm{m^{-2}\ s^{-1}\ TeV^{-1}}\ , \quad (E \text{ in TeV}) \quad (10)$$

The integral flux above 1 TeV is

$$I(>1\ \mathrm{TeV}) = (2.1 \pm 0.2 \pm 0.3) \times 10^{-7}\ \mathrm{m^{-2}\ s^{-1}}$$

if the flux is extrapolated by this preferred equation (10), and it is not significantly different if the power law is used (eq. [6]). The observed spectrum is close to the predicted flux of gamma rays due to inverse Compton scattering of (typically) infrared photons by multi-TeV electrons in the nebula, if the magnetic field in the region responsible for X-ray emission (from which we deduce the number of multi-TeV electrons) is ≈ 16 nT. The center of the soft X-ray emission, which is the region thus probed, is at a projected distance of 0.4 from the pulsar. Since this is widely interpreted as part of a torus inclined to the line of sight, it is probably equivalent to a distance of 0.4 pc. There are some indications—from the position of one of several breaks in the synchrotron spectrum, as discussed in § 3—that the magnetic field in the main part of the nebula may be appreciably larger than this, but at present the evidence on this point is very weak, and the evidence of the scattered gamma-ray flux suggests that the common assumption of energy equipartition overestimates the magnetic field strength. If indeed the main magnetic field is not be very different from 16 nT, inverse Compton scattering would be a satisfactory explanation also for the EGRET observations of GeV photons.

Measurement of TeV fluxes thus has the potential to probe the spatial variation of magnetic field strength in synchrotron sources, and the spectrum of the Crab Nebula above 10 TeV already probably shows an appreciably smaller magnetic field strength, best explained by their parent electrons only existing closer to the accelerating shock. It does not appear possible, however, to use the inverse Compton spectrum to test the poorly known magnetic field in the large volume occupied by electrons of tens of GeV, as the scatterd photons would be submerged in the high flux of synchrotron photons below 0.2 GeV.

Returning to the measurement techniques, since agreement is obtained using alternative simulations and alternative calibrations, and using data taken several years apart, with a telescope that had been subjected to several changes, we conclude that gamma rays of 0.5–5 TeV can be detected by present techniques with stable and known efficiency, and the stable flux of gamma rays from the Crab Nebula can be used as a calibration source for TeV detectors.

We would like to thank Kevin Harris, Teresa Lappin, and Carol Ward for technical assistance in obtaining our data. Alice Harding is also thanked for helpful information about predicted and observed gamma-ray spectra, and Okkie de Jager is thanked for further suggestions. This research was supported by the US Department of Energy, by NASA grants from *CGRO*, by PPARC in the UK, and by Forbairt in Ireland. A. M. H., H. J. R., and T. C. W. acknowledge the award of a NATO travel grant.

APPENDIX A

INTEGRATION OF THE ENERGY SPECTRUM

If the differential energy spectrum is written in the form $-dI/dE = AE^{-g-b \ln E}$, as in equation (8), the integral number of photons above energy E is

$$I(E) = \frac{A}{(2b)^{1/2}} e^{\Gamma^2/4b} \int_{t_0}^{\infty} e^{-1/2\, t^2}\, dt \ ,$$

where $\Gamma = g - 1$, and $t_0 = (2b)^{1/2} \ln E + \Gamma(2b)^{1/2}$. In the case of $E = 1$ (integral flux >1 TeV),

$$I(1) = \frac{A}{\Gamma}\left[1 - \frac{2b}{\Gamma^2} + \frac{12b^2}{\Gamma^4} - \cdots\right].$$

In the case $A = 3.25 \times 10^{-7}$, $g = 2.44$, and $b = 0.151/\ln 10$, one finds $I(1) = 2.14 \times 10^{-7}$.

APPENDIX B

MORE DETAILS OF THE CALCULATIONS IN § 3

The flux of synchrotron radiation from the Crab Nebula has been expressed in the form of power laws in energy covering limited ranges of energy. Thus, between photon energies ϵ_i and ϵ_j,

$$vF_v = \epsilon^2\, d^3N/d\epsilon\, dt\, dA = P_j(\epsilon/\epsilon_j)^{\delta} \mathrm{W m^{-2}} \ .$$

Here $d^3N/d\epsilon\, dt\, dA$ is the number of photons received per unit time, area, and photon energy. The expression above is thus the power received per unit area per unit interval of ln ϵ. Table 1 gives values of ϵ_j, P_j, and δ_j that are proposed here to define the spectrum. In the table, ϵ_i and ϵ_j are given in electron volts. The upper and lower halves of the table refer to the upper and lower limiting forms assumed for the synchrotron spectrum reaching Earth. A further factor $1.0/[1 + (\epsilon/110\ \mathrm{MeV})^5]$ is applied at high energies to give a rapid falloff above 100 MeV.

In order to derive the energy spectrum of electrons in the nebula, this spectrum, dN_e/dE, was also expressed as segments of power-law form, the function being continuous where the slope changed. A first estimate was obtained using a δ-function approximation to the synchrotron radiation process. Then, the synchrotron spectrum that would result was computed by numerical evaluation of the following expression for the power emitted per Hz in a magnetic field B:

$$P_v(v) = \tfrac{1}{4}\sqrt{3}\,\alpha mc^2 \int_{\cos\theta=-1}^{\cos\theta=1} \left[\int_{s=0.001}^{s=8} (B/B_c)\, \sin\theta (dN_e/d\ln E) F(s) d\ln s\right] d\cos\theta \ , \tag{B1}$$

where α is the fine-structure constant, $B_c = 4.414 \times 10^9$ T (4.414×10^{13} G), and $F(s)$ is the well-known synchrotron function, with $s = v/v_{\mathrm{crit}}$. v_{crit} depends on E and $B \sin\theta$, so that in the second integral, $dN_e/d\ln E$ is evaluated for electron energy E, which is a function of s:

$$E = \sqrt{\frac{2hvmc^2 B_c}{3B \sin\theta s}} \ . \tag{B2}$$

The intensity of each segment of the electron spectrum was adjusted to give the best average prediction for the synchrotron flux at frequencies radiated by electrons in that segment, and the "join-point energies" of the segments were changed to match the intersection points of these adjusted segments. In the end, the rms discrepancy between the computed synchrotron flux arising from the electron spectra and the observed synchrotron flux was about 4%, excluding a rounding that occurred very close to some of the artificially sharp bends in the synchrotron spectrum as it is represented here. The change from the original δ-function approximation was about 40%. The input synchrotron spectrum and the deduced electron spectra were shown in Figure 4, and the electron spectrum deduced for the case $B = 16$ nT is shown in Table 2. In each segment, the total number of

TABLE 1

SYNCHROTRON SPECTRUM ASSUMED IN CALCULATION

HI/LO[a]	Segment	ϵ_i	ϵ_j (eV)	P_j (W m^{-2})	δ	Integrated Power (W m^{-2})
HI	1	1.0×10^{-8}	3.92×10^{-2}	7.35×10^{-12}	0.725	1.01×10^{-11}
HI	2	3.92×10^{-2}	7.25	3.34×10^{-11}	0.29	9.0×10^{-11}
HI	3	7.25	1.0×10^{5}	6.0×10^{-12}	−0.18	1.52×10^{-10}
HI	4	1.0×10^{5}	1.0×10^{9}	2.39×10^{-13} [b]	−0.35[b]	1.65×10^{-11}
HI	5	1.0×10^{9}	1.0×10^{12}	4.77×10^{-16} [b]	−0.9[b]	...
LO.....	1	1.0×10^{-8}	3.92×10^{-2}	7.35×10^{-12}	0.725	1.01×10^{-11}
LO.....	2a	3.92×10^{-2}	1.0	1.88×10^{-11}	0.29	...
LO.....	2b	1.0	1.0×10^{3}	1.53×10^{-11}	−0.03	...
LO.....	3b	1.0×10^{3}	1.0×10^{5}	6.0×10^{-12}	−0.18	...
LO.....	4	1.0×10^{5}	1.0×10^{9}	2.39×10^{-13} [b]	−0.35[b]	...
LO.....	5	1.0×10^{9}	1.0×10^{12}	4.77×10^{-16} [b]	−0.9[b]	...

[a] Using upper or lower limit of assumed visible–to–X − ray synchrotron spectrum

[b] Above 70 MeV the rapid falloff term greatly modifies the flux.

TABLE 2

ELECTRON SPECTRUM DEDUCED FOR THE CASE $B = 16$ nT

HI/LO[a]	Segment	E_i (eV)	E_j (eV)	$(dN_e/d\ln E)_j$	β	Integrated Energy (J)
HI	1	1.0×10^9	1.14×10^{11}	6.93×10^{48}	−0.55	2.81×10^{41}
HI	2	1.14×10^{11}	9.6×10^{11}	3.36×10^{47}	−1.42	1.78×10^{41}
HI	3	9.6×10^{11}	1.01×10^{14}	5.69×10^{42}	−2.36	3.8×10^{40}
HI	4	1.01×10^{14}	3.0×10^{15}	5.95×10^{38}	−2.70	5.4×10^{37}
LO.....	1	1.0×10^9	1.20×10^{11}	6.73×10^{48}	−0.55	2.89×10^{41}
LO.....	2a	1.20×10^{11}	3.40×10^{11}	1.53×10^{48}	−1.42	1.11×10^{41}
LO.....	2b	3.40×10^{11}	1.05×10^{13}	1.17×10^{45}	−2.09	7.5×10^{40}
LO.....	3b	1.05×10^{13}	1.02×10^{14}	5.50×10^{42}	−2.36	1.4×10^{39}
LO.....	4	1.02×10^{14}	3.0×10^{15}	5.95×10^{38}	−2.70	5.3×10^{37}

[a] Using upper or lower limit of assumed visible–to–X-ray synchrotron spectrum

electrons in the nebula at energy E between E_i and E_j may be expressed in the dimensionless form $dN_e/d\ln E = (dN_e/d\ln E)_j (E/E_j)^{\beta}$. The spectrum is zero above 3.0 PeV. In this table, the figures assume a distance of 2 kpc for the Crab Nebula, and electron numbers scale as the square of distance.

The total energy carried by these electrons is 4.97×10^{41} or 4.76×10^{41} J in the upper or lower limits, respectively. This is less than $\frac{1}{10}$ of the present rotational energy of the Crab pulsar.

One can compare this energy with that stored in the magnetic field if some defining volume is assumed for the magnetic field. As the extent of the field is very critical in this estimate, it is more realistic for this purpose to assume that the magnetic field dies away with increasing distance in the same way as does the particle energy. Thus if, as assumed before, the particle density varies as $e^{-(r/\rho)^2/2}$, the magnetic energy density will be assumed to vary in the same way, so $B = B_0\, e^{-(r/\rho)^2/4}$. Since one finds from equation (B1) the result that $P_\nu \propto B^{1.27}$ in the case where $P_\nu \propto \nu^{-0.27}$, as in the radio domain, the synchrotron emission rate will vary with distance as $e^{-1.27(r/\rho)^2/4 - (r/\rho)^2/2}$. Equating this to $e^{-(r/\sigma)^2/2}$ as defined in the main text, one finds that $\rho = 1.28\ \sigma = 1.00$ pc. The total magnetic energy $k \int 4\pi r^2 B^2(r)\, dr = kB_0(\rho\pi^{1/2})^3$, where k is $10^7/8\pi$ if B is in tesla (SI units) or $1/8\pi$ for cgs-gauss units. Hence, if the magnetic field had the same energy as the relativistic electrons, $B_0 = 50$ nT. With this geometry, the weighted average value of B weighted by the synchrotron emissivity would be $0.67B_0$, so $B_{\rm average} = 34$ nT.

The inverse Compton spectrum is derived as follows.

1. Scatterings of photons by electrons are first generated with a constant cross section $\sigma_0 = \pi r_0^2$, r_0 being the classical radius of the electron, these occurring at a rate $\int_{E_{\rm elec}} \int_{E_{\rm phot}} \int_{\psi} (dN_e/d\ln E_{\rm elec})(dn_{\rm phot}/dE_{\rm phot})\sigma_0\, c(1 - \cos\psi)^{\frac{1}{2}}\, d\cos\psi\, d\ln E_{\rm phot}\, d\ln E_{\rm elec}$. This process is simulated by drawing electrons from the specified spectrum $dN_e/d\ln E_{\rm elec}$, in practice by (*a*) selecting values of $\ln E_{\rm elec}$ randomly from the whole range of $\ln E_{\rm elec}$ and giving the sample a weight $w = dN_e/d\ln E_{\rm elec}$; (*b*) then making an analogous sampling of $\ln E_{\rm phot}$ with its weight w' and multiplying w by w'; (*c*) selecting at random a value of $\cos\psi$, where ψ is the angle between the momenta of the electron and photon in this global frame of reference. The photon's energy and momentum are then transformed to the rest frame of the electron, and an outgoing direction for the scattered photon is chosen isotropically in this initial rest frame of the electron.

2. The above process simulates isotropic scattering with a constant cross section, and the rate for this has to be corrected. If the photon had an energy $E_{{\rm phot},e}$ in the electron's rest frame and was deflected through an angle θ in this frame, the rate for each scattering is then multiplied by the factor $4\pi c(1 - \cos\psi)\sigma_{\rm KN}(E_{{\rm phot},e}, \theta)/\sigma_0$. Here, $\sigma_{\rm KN}(E_{{\rm phot},e}, \theta)$ is the Klein-Nishina differential cross section per unit solid angle. For each simulated encounter, a Lorentz transformation of the photon's energy back to the global frame gives its final energy. Each simulated encounter thus has an attached weight, and accumulating the weights of all the outgoing photons in suitable energy "bins" gives the rate of production of scattered photons in each of these energy ranges, after normalizing for the total number of samples taken. The results are as shown in Figure 5.

APPENDIX C

BREAK POINT IN SPECTRUM

We first assume that electrons are produced at a constant rate $d^2N/dE\, dt = QE^{-\gamma}$. To match the radio spectrum of the Crab Nebula, $\gamma = 1.54$. If the production has continued for a time T ($\sim$940 yr), and the electrons lose energy by synchrotron radiation at a rate $-dE/dt = (E/E_s)^2(E_s/T)$, then E_s marks the energy above which no particles survive from the earliest production time. In the simplest case of constant production, and no other energy losses, the spectrum of particles present now is $dN/dE = QT\ E^{-\gamma}$ at energies well below E_s, and $dN/dE = QT[E^{-\gamma}/(\gamma - 1)]E_s/E$ at $E > E_s$. These two power-law spectra intersect at a "join-point energy" $E_j = E_s/(\gamma - 1)$. Although there is an excess flux just below E_j, numerical integration of the resulting synchrotron spectrum confirms that this does not result in an appreciable excess in the synchrotron spectrum, so this join point effectively determines where the synchrotron spectrum breaks. The electron spectra deduced for different field strengths show a sharp break (between segments 1 and 2) at an energy $E_j = 455\ {\rm GeV}\,(B_{\rm nT})^{-1/2}$. On substituting $E_s = 1.25 \times 10^{17}{\rm eV}/(T_{\rm yr}\, B_{\rm nT}^2)$, one finds that $E_j = E_s/0.55$ if $B \sim 65$ nT. A full numerical treatment of the synchrotron spectrum from electrons produced at uniform rate with the appropriate simple power-law spectrum gives the spectral break at

10^{13} Hz if $B = 60$ nT. Changes occurring during the lifetime of the nebula can alter this estimate, but such changes usually alter the change in spectral slope, which is observed to be close to the value 0.5 (in the synchrotron spectrum) expected for the simple case. Allowance for adiabatic expansion losses does not reduce the estimated field strength.

REFERENCES

Aharonian, F. A., & Atoyan, A. M. 1995, Astropart. Phys., 3, 275
Arons, J. 1996, Space Sci. Rev., 75, 235
Aschenbach, B., & Brinkmann, W. 1975, A&A, 41, 147
Atoyan, A. M., & Aharonian, F. A. 1996, MNRAS, 278, 525
Bartlett, L. M., Barthelmy, S. D., Gehrels, N., Teegarden, B. J., Tueller, J., Leventhal, M., & MacCallum, C. J. 1994, in AIP Conf. Proc. 304, The Second Compton Symposium, ed. C. E. Fichtel, N. Gehrels, & J. P. Norris (New York: AIP), 67
Borione, A., et al. 1997, ApJ, 493, 175
Coroniti, F. V., & Kennel, C. F. 1985, in The Crab Nebula and Related Supernova Remnants, ed. M. C. Kafatos & R. B. C. Henry (Cambridge: Cambridge Univ. Press), 35
de Jager, O. C., & Harding, A. K. 1992, ApJ, 396, 161
de Jager, O. C., Harding, A. K., Michelson, P. F., Nel, H. I., Nolan, P. L., Sreekumar, P., & Thompson, D. J. 1996, ApJ, 457, 253
Djannati-Atai, A. 1995, Proc. 24th Int. Cosmic-Ray Conf. (Rome), 315
Gillanders, G.H., et al 1997, Proc. 25th Int. Cosmic-Ray Conf. (Durban), 3, 185
Gould, R. J. 1965, Phys. Rev. Lett., 15, 577
Grindlay, J. E., & Hoffman, J. A. 1971, Astrophysics Lett., 8, 209
Harnden, F. R., Jr., & Seward, F. D. 1984, ApJ, 283, 279
Hester, J. J., et al. 1995, ApJ, 448, 240
Hillas, A. M., & West, M. 1991, Proc. 22d Int. Cosmic-Ray Conf. (Dublin), 6, 472
Hillas, A. M. 1995, Proc. 24th Int. Cosmic-Ray Conf. (Rome), 1, 270
Kardashev, N. S. 1962, Soviet Astron. 6, 317
Kaye, G. M., & Laby, T. H. 1995, Tables of Physical and Chemical Constants (16th ed.; Essex, UK: Longman), 198
Kennel, C. F., & Coroniti, F. V. 1984a, ApJ, 283, 694
———. 1984b, ApJ, 283, 710
Kertzman, M. P., & Sembroski, G. H. 1994, Nucl. Instrum. Methods A, 343, 629
Konopelko, A., et al. 1996, Astropart. Phys., 4, 199
Kundt, W., & Krotschek, E. 1980, A&A, 83, 1
Kwok, P. W. 1989, Ph.D. thesis, Univ. Arizona
Kwok, P. W., Cheng, K. S., & Lau, M. M. 1991, ApJ, 379, 653
Lewis D. A., et al. 1993, Proc. 23d Int. Cosmic-Ray Conf. (Calgary), 1, 279
Marsden, P. L., et al. 1984, ApJ, 278, L29
Michel, F. C. 1985, in The Crab Nebula and Related Supernova Remnants, ed. M. C. Kafatos & R. B. C. Henry (Cambridge: Cambridge Univ. Press), 55
Mohanty, G. 1995, Ph.D. thesis, Iowa State Univ.
Mohanty, G., et al. 1998, Astropart. Phys., in press
Nolan, P. L., et al. 1993, ApJ, 409, 697
Petry, D., et al. 1996, A&A, 311, L13
Punch, M., et al. 1991, Proc. 22d Int. Cosmic-Ray Conf. (Dublin), 1, 464
Rees, M. J., & Gunn, J. E. 1974, MNRAS, 167, 1
Reynolds, P. T., et al. 1993, ApJ, 404, 206
Rieke, G. H., & Weekes, T. C. 1969, ApJ, 155, 429
Stepanian, A. A. 1980, Izv. Krymskoi Astrofiz. Obs., 62, 79
———. 1990, in Vulcano Workshop 1990: Frontier Objects in Astrophysics and Particle Physics, ed. F. Giovannelli & D. Mannocchi (Bologna: IPS), 377
———. 1995, Nucl. Phys. B (Proc. Suppl.), 39A, 207
Tanimori, T., et al. 1998, ApJ, 492, L33
Trimble, V. 1968, AJ, 73, 535
Vacanti, G., et al. 1991, ApJ, 377, 467
Weekes, T. C., et al. 1989, ApJ, 342, 379
West, M. 1994, Ph.D. thesis, Univ. Leeds
Wilson, A. S. 1972, MNRAS, 157, 229
Wilson, A. S., Samarasinha, N. H., & Hogg, D. E. 1985, in The Crab Nebula and Related Supernova Remnants, ed. M. C. Kafatos & R. B. C. Henry (Cambridge: Cambridge Univ. Press), 133
Woltjer, L. 1957, Bull. Astron. Inst. Netherlands, 13, 301